Formatted: Font: (Default) +Body (Times New Roman)

Microscale Alkenone Heterogeneity and Replicability of Ultra-High-Resolution Temperature Records from Marine Sediments

Jannis Viola[1,2], Lars Wörmer[2], Kai-Uwe Hinrichs[2], Thomas Laepple[1,2]

[1]Alfred-Wegener-Institut, Helmholtz Center for Polar and Marine Research, Potsdam, D-14473, Germany
[2]University of Bremen, MARUM – Center for Marine Environmental Sciences and Faculty of Geosciences, Bremen, D-28334, Germany

Correspondence to: Jannis Viola (jannis.viola@awi.de)

Formatted: Heading 2

Abstract. The alkenone-derived $U^{K'}_{37}$ proxy is crucial for the reconstruction of past sea surface temperatures in marine sedimentary archives. Recent advances in mass spectrometry imaging (MSI) now allow to measure alkenone abundance at the micrometer scale. Such an approach can theoretically provide proxy records as highly resolved as observational records and hold the promise of continuously reconstructing climate variability from subseasonal or interannual to centennial and millennial timescales. However, due to processes occurring during and after deposition, as well as during sampling and measurement, it is unclear how much climate signal is preserved in the proxy signal at these small spatial scales. Here, we investigated this question on sediment records from the Santa Barbara Basin (SBB), off California. We performed replicated MSI measurements on sediments with varying degrees of lamination to analyze the spatial structure and spatial reproducibility of the alkenone signal. We find that alkenone distributions are spatially heterogeneous even within laminae but exhibit small scale clustering over the range of ~0.5-1 mm. Measurements along laminated horizons show longer ranges of similarity and less overall variability compared to measurements across depth. Signal to noise ratios (SNR), the amount of shared variance between proxy records derived from the replicates across varying sediment conditions range from ~1 SNR at interannual resolution to ~3 SNR at subdecadal timescales and provide an upper limit for the potential climate signal content of individual time series at these timescales.~~s.~~

MSI-based $U^{K'}_{37}$ records in the SBB, supported by careful estimation of noise and uncertainty, thus can capture subdecadal SST variability and provide an upper limit for the signal content of Holocene and late Pleistocene SST reconstructions.

~~-~~The approach presented here can be used in other settings to infer optimal sampling and measurement resolution~~,~~ as well as to provide uncertainty estimations for the proxy records.

1 Introduction

Understanding past climate and its dynamics is crucial for contextualizing recent climate change and processes in warmer-than-present climate states under projected future conditions.~~Understanding past climate and its dynamics is crucial for contextualizing recent climate change and projected future conditions.~~ Sea surface temperature (SST) is an essential climate variable (Bojinski et al., 2014), but reliable SST observations only cover the last 150 years (Huang et al., 2017). Therefore, the instrumental record is too short to fully characterize climate variability at decadal or ~~slower~~ longer timescales (Ault et al., 2013; Laepple and Huybers, 2014). Similarly, to gain a better understanding of the long-term dynamics of phenomena such as monsoons or the El Niño–Southern Oscillation (ENSO), records are required that can resolve interannual variability over longer time periods~~Similarly, to gain a better understanding of the long-term dynamics of phenomena like monsoon or El Niño–Southern Oscillation (ENSO), records are required that can resolve interannual variability over longer time periods~~ (Huang et al., 2017). Marine sediments offer such long, continuous archives, and~~,~~ in the case of laminated sediments, represent a key resource when aiming for the highest possible resolution (Hathorne et al., 2023; Schimmelmann et al., 2016). Recent technological advances in ultra-high-~~-~~resolution methods such as µXRF geochemical spatial scans (Blanchet et al., 2021), hyperspectral imaging (Butz et al., 2015; Zander et al., 2022) as well mass spectrometry imaging (MSI) (Alfken et al., 2020; Napier et al., 2022; Obreht et al., 2022a; Wörmer et al., 2014, 2022) offer the potential to interrogate these archives with a spatial resolution leading to near-annual timescales while covering long-~~-~~enough intervals to capture the influence of slower variations of the climate system.

In traditional proxy studies, sampling resolution (mm to cm) typically exceeds archive accretion rates (de Winter et al., 2021). This might, however, not be the case for the microscale methods mentioned above, where theoretical resolution ~~might~~ can exceed the actual temporal resolution at which proxies record climate signals. The temporal resolution and inter-record replicability of proxies can also be also affected by microscale heterogeneity in sediments or signal carriers~~–~~. Such heterogeneity may arise during signal production, for example, due to heterogeneous SST patterns, eddies, surface mixing, or variations in habitat depth. In marine settings, variability can also stem from differences in sinking rates, advection, and lateral transport. Post-depositional processes like bioturbation,~~—~~ even under low-oxygen conditions,~~—~~ can further alter the signal (Bernhard et al., 2003), introducing non-climatic variability similar to ‘stratigraphic noise’ (Fisher et al., 1985) in ice climate archiv~~i~~es, which reduces the reliability of single-proxy climate reconstructions (Münch et al., 2016). Bioturbation and sediment mixing can, for example, smooth temperature signals (Anderson, 2001; Hülse et al., 2022; Liu et al., 2021; Schiffelbein, 1984), leading to loss of resolution and dampening of high-frequency variability (Münch and Laepple, 2018). 2D methods that map the distribution of the signal carriers harbor the potential to estimate the spatial variability of the signal of the otherwise discretely sampled or line-scanned proxies, ultimately deriving estimates of the proportion of climate variability captured.

In this study, we focus on long-chain alkenones produced by haptophyte algae. The alkenone-based $U^{K'}_{37}$ (Brassell et al., 1986; Prahl et al., 1988; Prahl and Wakeham, 1987) is a well-established SST proxy with global spatial and long temporal coverage. Additionally, we investigate pyropheophorbide *α*,~~—~~ a chlorophyll degradation product (Goericke et al., 2000),~~—~~ as a first-order proxy for ~~primary~~ export productivity. The sediment cores used are from the Santa Barbara Basin (SBB), offshore Southern California.

Seasonal runoff, high primary productivity, and the basin's bathymetry allow for the formation of laminae or annual varve couplets and for their preservation under low-oxygen conditions due to drastically reduced bioturbation (Schimmelmann and Lange, 1996; Thunell et al., 1995). Past variations in bottom-water oxygen levels resulted in varying bioturbation intensities, ranging from merely submillimeter disturbance, which allows for the preservation of varves (Bernhard et al., 2003), to complete mixing following colonization by larger fauna (Anderson et al., 1989).

~~Seasonal runoff, high primary productivity, and the basin's bathymetry allow for the formation of laminae or annual varve couplets, and for their preservation under low-oxygen conditions that reduce bioturbation (Schimmelmann and Lange, 1996;~~

~~Thunell et al., 1995)(Bernhard et al., 2003). Past variations in bottom-water oxygen levels resulted in varying bioturbation intensities, from minimal disturbance that preserved varves(Bernhard et al., 2003) to complete mixing after colonization by larger fauna (Anderson et al., 1989).~~ We present spatially resolved alkenone measurements at 100 µm resolution to characterize the spatial heterogeneity of the biomarkers in relation to lamina preservation~~,~~ from well-preserved to mixed intervals. Mixing and bioturbation intensities assessed in this study are representative for the Holocene and late Pleistocene SBB sediments (Anderson et al., 1990; Behl, 1995). We then assess the influence of microscale heterogeneity on noise level and replicability of MSI-derived high-resolution $U_{37}^{K'}$ SST proxies. Subsequently, we estimate signal-to-noise ratios (SNR) of individual MSI-based reconstructions, which indicate the finest usable proxy time series resolution based on the sediment structure.

2 Materials and Methods

2.1 Samples, Sample Processing and Measurements

Sediment core MV1012-001KC was retrieved by research vessel Melville during cruise MV1012 in 2012 and subsequently~~,~~ stored and accessed at the Scripps Institution of Oceanography's~~ cored~~ sediment core and microfossil collection. We used a 30-cm~~-~~long section of this core, ~~named~~ referred to as "KC1" ~~in the following~~for the remainder of this manuscript. Depths are expressed as relative centimeters,~~m~~ starting at the top of the sampled section. We additionally utilized data ~~of~~ from three 5~~-~~ cm replicated MSI measurements (approx. years 1913-1935) of boxcore SPR0901-05BC, originally published by Alfken et al. (2020), as an example ~~for~~ of well-preserved varved deposition with known correlation to the instrumental record, named "SBX" in the remainder of the study. The sediment samples were treated following the procedure developed~~escribed~~ by Alfken et al. (2019), an additional description of laboratory and processing workflows can be found in Zander et al. (~~Zander et al.,~~ 2026). ~~In brief~~Briefly, after subsampling, X-ray photographs of the wet 30 cm sediment slabs (Fig. 1, step 1) were ~~taken~~ obtained using a Faxitron 43855A X-ray cabinet (Hewlett-Packard). 5~~-~~ cm subsections were freeze~~-~~dried and embedde~~d~~d in an aqueous gelatine~~e~~:CMC (4%:1%) solution (g~~G~~elatin~~e~~ from porcine skin, gel strength 300, type A and sodium carboxymethylcellulose, Sigma-Aldrich Chemie GmbH, Munich Germany, see Fig. 1, steps 1-2). After freezing ~~of~~ the embedded samples, they were cut into 100-µm slices using a cryomicrotome (Medite Cryostat M630), ~~-~~and the slices were placed on indium-tin-oxide coated (ITO) glass slides (Bruker Daltonik GmbH, Bremen, Germany~~,)~~ see Fig. 1, step 3). High-resolution RGB scans were performed as guidance for setting up the ~~-~~FT-ICR ~~-~~MS measurements. Finally, organic compounds between 554 m/z and 564 m/z on each of the slices were measured using a 7T solariX XR FT-ICR ~~-~~MS coupled to a LDI source equipped with a Smartbeam II laser (Nd:YAG, UV-A Laser, 355nm wavelength, Bruker Daltonik, Bremen). Details o~~n~~f the FT-ICR ~~-~~MS measurement settings can be found in section S1 of the supplemental materials.~~in the supplements section S1.~~

For each 5-cm depth interval of KC1 00-30 cm relative depth, the workflow was repeated on three subsequent slices, yielding triplicate measurements with the minimum achievable distance to the previous measurement area (100-µm cutting thickness).

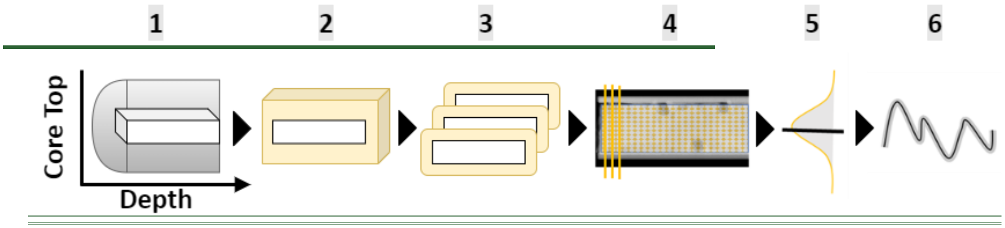

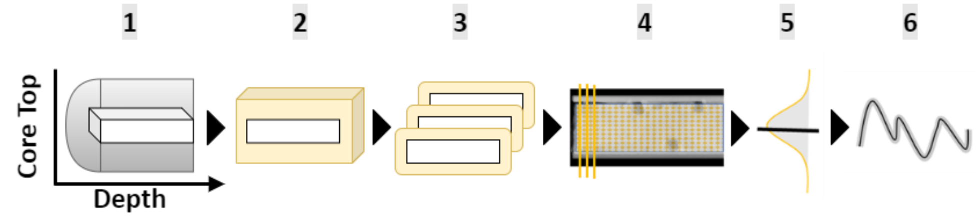

Figure 1: Schematic representation of the triplicate workflow. 1) Subsampling from sediment cores via 30cm LL-channels (Suigetsu 2006 Project Members and Nakagawa, 2014), used for X-ray photography; 2) freeze-drying and embedding of 5-cm subsections ("pieces"), 3) cryomicrotome cutting onto ITO slides of 3 subsequent 100-µm "slices" per piece; 4) MSI scans; 5) data processing, horizon-wise aggregation & conversion to time series; 6) time series analyses. Orientation of sediment samples and time series is left to right: core top ("recent") to depth ("past").

~~Figure 1: Schematic representation of the triplicate workflow. (Suigetsu 2006 Project Members and Nakagawa, 2014)1) 30-cm core LL-channel subsampling (Suigetsu 2006 Project Members and Nakagawa, 2014), used for X-ray photography; 2) freeze drying and embedding of 5-cm samples; 3) cryomicrotome cutting of 100-µm slices to be placed on ITO slides, 4) MSI scans, 5) horizon-wise aggregation & conversion to time series, 6) time series analyses.~~

The MSI measurements were inspected and lockmass calibrated using Bruker Compass DataAnalysis 5.0 SR1 (Bruker Daltonik Gmbh, 2017). Our main targets were the Na$^+$ adducts of the di- and tri-unsaturated alkenones (C37:2, C37:3). Each of the shots (orange dots in Fig. 1, step 4) resulted in a mass spectrum from which the intensities of the compounds, as well peak quality ("SNR$_{FT}$") were extracted and used for further analyses, either per spectrum (spotwise-calculated $U^{K'}_{37}$, "swUk") using the formula

Formatted: Font: Bold

Formatted: Font: Bold

Formatted: Font: Bold

Formatted: Font: Bold

Formatted: Font: Bold

Formatted: Subscript

$$U^{K'}_{37} = \frac{C37:2}{(C37:2 + C37:3)} \tag{1}$$

(Prahl and Wakeham, 1987) or aggregated per horizon (see Fig. 1, step 4-6 and section 2.5 Time-Series Analyses). Peak intensities were only used when passing a SNR$_{FT}$ quality threshold. Besides alkenones, we utilized pyropheophorbide *α* as a first-order estimation for primary production and calibrant during FT-ICR-MS lockmass calibration due to its ubiquity in SBB sediments (Liu et al., 2022) and stability over the timescales of this study (Szymczak-Żyła et al., 2011).

During the development of the MSI workflow by Wörmer et al, (Wörmer et al., 2014) and in subsequent studies, the resulting $U^{K'}_{37}$ values were verified using GC-FID measurements (Alfken et al., 2020; Napier et al., 2022; Obreht et al., 2022b, a). Differences in $U^{K'}_{37}$ values obtained by different mass spectrometry techniques have been reported and attributed to varying ionization efficiencies of alkenones, the co-elution of other compounds, and additional factors (Chaler et al., 2000, 2003; Liao et al., 2023; Rama-Corredor et al., 2018). Notably, data derived from MSI in warm SST regions have shown a cold bias compared to GC-FID data, leading to the introduction of site-specific correction factors. However, in the temperate SST regime of SBB, MSI and GC-FID data did not exhibit significant differences and correlated well with CalCOFI buoy SST data at the site (Alfken et al., 2020; California State Department of Fish and Game; NOAA Fisheries; Scripps Institution of Oceanography, 2001).

~~(Wörmer et al., 2014)(Alfken et al., 2020; Napier et al., 2022; Obreht et al., 2022b, a)(Chaler et al., 2000, 2003; Liao et al., 2023; Rama-Corredor et al., 2018)(Alfken et al., 2020; California State Department of Fish and Game; NOAA Fisheries; Scripps Institution of Oceanography, 2001)~~Calculated $U^{K'}_{37}$ values were then translated to temperature using the calibration of Prahl and Wakeham (1987). Other calibrations are available (Tierney and Tingley, 2018), yet the experimental calibration of Prahl and Wakeham was confirmed by Müller et al. (1998) for 60S-60N and the applicability of this calibration for California specifically was supported by Herbert et al. (1998). As our results focus on replicability, they are not sensitive to the choice of calibration.

~~For each 5 cm depth interval of KC1 00-30 cm relative depth, the workflow was repeated on three subsequent slices, yielding triplicate measurements with the minimum achievable distance to the previous measurement area (100 µm cutting thickness) (see Fig. 1).~~

~~The MSI measurements were inspected and lockmass calibrated using Bruker Compass DataAnalysis 5.0 SR1 (Bruker Daltonik Gmbh, 2017). Our main targets were the Na^{+} adducts of the di- and triunsaturated alkenones (C37:2, C37:3). {Citation}Calculated $U^{K'}_{37}$ values were translated to temperature using the calibration of Prahl and Wakeham (1987). Other calibrations are available (Tierney and Tingley, 2018), yet the experimental calibration of Prahl and Wakeham was confirmed by Müller et al. (1998) for 60S-60N and the applicability of this calibration for California specifically was supported by Herbert et al. (1998). As our results focus on replicability, they are not sensitive to the choice of calibration. Besides alkenones, we utilized pyropheophorbide α as a first order estimation for primary production and calibrant during FT-ICR-MS lockmass~~

~~calibration due to its ubiquity in SBB sediments (Liu et al., 2022) and stability over the timescales of this study (Szymczak-Żyła et al., 2011).~~

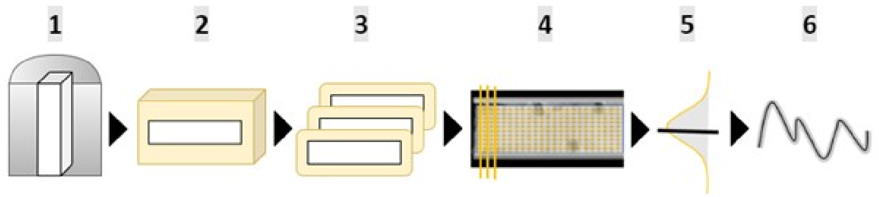

~~**Figure 1: Schematic representation of the triplicate workflow. 1) 30-cm core LL-channel subsampling (Suigetsu 2006 Project Members and Nakagawa, 2014), used for X-ray photography; 2) freeze drying and embedding of 5-cm samples; 3) cryomicrotome cutting of 100-µm slices to be placed on ITO slides, 4) MSI scans, 5) horizon-wise aggregation & conversion to time series, 6) time series analyses.**~~

2.2 Study Area

The Santa Barbara Basin is located in the Southern California Bight and part of the California Current System (Bograd et al., 2019). The basin covers ~110 km² and is separated from the Pacific in the west and the Santa Monica Basin in the east by submarine sills, with the depocenter at ~595m (Soutar and Crill, 1977). The bathymetric layout, together with seasonal upwelling, high productivity in summer, and high sedimentation rates from winter runoff, can favor the preservation of laminated or ~~even~~ varved sediments (Reimers et al., 1990; Thunell et al., 1995). The sediment sequence is interrupted by flood layers ("gray layers") and mass movements from the upper shelf close to the shore ("massive olive layers"), and bioturbated intervals (Du et al., 2018; Hendy et al., 2013). Oxic time intervals allow ~~the~~ colonization by~~with~~ macrofauna, for example, during the Macoma event 1835-1840 (Schimmelmann et al., 1992). During the Holocene and Late Pleistocene, varved, laminated, or bioturbated sections alternated in response to phases of varying oxygenation (Anderson et al., 1990). However, Bernhard et al. (~~Bernhard et al.,~~ 2003) reported microscale bioturbation even under~~in~~ oxygen-~~-~~limited or anoxic-sulfidic conditions.

2.3 Age Control

~~For this study, we focused on a sediment section that includes both partially laminated and mixed intervals, beginning around the 1761 AD flood layer (Hendy et al., 2013). The presence of a massive olive-colored layer and partially mixed sections below prevented the development of a detailed age model beyond linear interpolation between the 1761 AD and 1532 AD gray flood layers, following approaches such as Zhao et al. (Zhao et al., 2000) and O'Mara et al. (O'Mara et al., 2019). As a result,~~

Formatted: Highlight

~~we conducted our analyses on a depth scale, which also enhances the comparability of our results across different depths and sediment structures within the Santa Barbara Basin.~~

We conducted our analyses on depth scale, as the focus was on replicability, which is independent of an exact age scale, and depth- or distance-based interpretations enhance the comparability of our results across different depths and sediment structures within the SBB. For general orientation, we anchored our sediment section KC1 to existing chronologies by identifying flood and event layers in the X-ray imagery (see Supplements S2). The topmost 0-5 cm relative depth piece contains a flood layer that aligns with the 1761AD flood layer in SBB (Hendy et al., 2013). The presence of a massive olive-colored layer and partially mixed sections prevented the development of a detailed age model beyond linear interpolation between the 1761 AD and 1532 AD gray flood layers following approaches such as Zhao et al. (2000) and O'Mara et al. (2019). As a first-order age model to help interpret results of the spectral analyses, we used the reported average sedimentation rates of 1.4 mm/yr (Thunell et al., 1995).

Formatted: Not Highlight

Formatted: Not Highlight

Formatted: Not Highlight

Formatted: Not Highlight

Formatted: Not Highlight

Formatted: Not Highlight

Formatted: Heading 2

2.4 Spatial Analyses

We estimated the spatial correlation structure of the measured compounds and spotwise-calculated $U^{K'}_{37}$ ("swUk") temperatures using variogram analysis (Cressie, 1993; Maroufpoor et al., 2020; Wikle et al., 2019). For each starting point, "shot" in our case, the semivariance γ between the starting point and all other points in specific distance bins was calculated. We compared differences in horizontal (within horizon, approximately parallel to lamina, see orange lines in Fig. 1, step 4) and vertical (downcore) spatial (dis)similarity. Separating by direction enables~~ to~~ the characterization of~~quantify~~ ~~the~~ zonal and geometric anisotropy, which is the directional dependence of the total variance or its increase over distance, which can be used to~~, to~~ assess the influence of lamina preservation and the homogeneity of deposited horizons. Peak ~~I~~intensities of alkenones and pyropheophorbide α were log10 transformed, scaled, and centered to account for the strong non-normality of the data, ~~while~~ whereas spotwise $U^{K'}_{37}$ (swUk) values were used without transformation. For the estimation of the sample variogram, we used ~~a~~the R::gstat implementation (Gräler et al., 2016; Pebesma, 2004; Posit team, 2025; R Core Team, 2024)~~,(Posit team, 2025; R Core Team, 2024)~~ choosing 100 µm bin widths, together with horizontal and vertical tolerance of 10° to ensure sufficient data coverage and account for deviations in sample or laminae orientation.

Formatted: Heading 2

2.5 Time-series Analyses

MSI data was mapped to the X-ray density maps using three tie points and an affine transformation to correct for potential sample deformation during embedding and cutting (Alfken et al., 2020) using the P~~p~~ython software msiAlign (Liu et al., 2025). The known flood layer in the upper part of the KC1 segment was identified using X-ray density scans and MSI data, and the respective subsection was excluded from the 0-5 cm interval replicates prior to statistical analyses. Horizons with very low numbers of MSI detections across all compounds (fewer than 10 simultaneous detections of C37:2 and C37:3) were~~ also~~ removed. To avoid introducing gaps and ~~to ~~ensure sufficient detections per horizon, the minimum horizon width was set to 200 µm. The time series were then formed by summing the intensities of each of the valid alkenone detections (simultaneous detection of both alkenones per shot, where each passes the SNR_{FT} threshold) within each horizon and calculating the $U^{K'}_{37}$. Short segments of missing horizons due to insufficient detections were linearly interpolated. On average, ~4% of horizons were missing: ~1.4% at the ends of series~~ ends~~ and ~2.7% within.

Following Laepple and Huybers (2014), power spectral density (PSD) estimates were calculated on linearly detrended, centered data using the multitaper method with three tapers and a time-bandwidth parameter of ω = 2 (Thomson, 1982). The PSD estimates were smoothed using a Gaussian kernel with a constant width of 0.2 on the logarithmic timescale (base 10) (Kirchner, 2005), and the three lowest and highest frequencies were omitted.

We followed the framework developed by Münch and Laepple (2018), based on a partitioning of variance approach (Fisher et al., 1985), to separate the climatic signal and noise contributions in the spectral domain. We defined the climate signal as the common signal shared between the time series of a depth interval. The residual, individual variations formed the noise component and allowed the quantification of the shared signal as signal-to-noise ratios.

Given a regional cluster of n proxy records with a similar climate between sites, the mean power spectrum, M, averaged across all individual records' spectra, will yield a precise estimate of the proxy spectrum. ~~Given *n* sediment slices that share a common signal, the mean power spectrum, *M,* computed by averaging the individual spectra of all slices, provides a precise estimate of the underlying can correspond to proxy spectrum *P*. ~~In contrast, the power spectrum~~,~~ *S*~~,~~ of the stacked record from averaging all datasets in the time domain~~,~~ will also contain the full common signal, but with the noise proportions reduced by a factor of *n*. By combining both quantities one can derive expressions for the climate and noise spectra (McPartland et al., 2024; Münch and Laepple, 2018)

$$\mathcal{C} = \frac{n}{n-1}(\mathcal{S} - \mathcal{M}/n) \tag{$\cancel{1}2$}$$

$$\mathcal{N} = \frac{n}{n-1}\left(\mathcal{M} - \mathcal{S} - \frac{n-1}{n}\right) \tag{$3\cancel{2}$}$$

with the ratio of *C:N* yielding the frequency-resolved signal-to-noise ratio (SNR). We further compute the integrated SNR which yields~~as equals~~ the SNR of the time-series that one obtains if one measures at a~~some~~ specific sampling resolution

$$iSNR_{f(Nyq)} = \frac{\int_0^{fNyq} C_f}{\int_0^{fNyq} N_f} \tag{$4\cancel{3}$}$$

The relation of SNR to correlation can be found in the supplements (S3), however as direct climatic interpretation is not the focus of this study, we report shared signal content between replicates expressed as SNR throughout the manuscript.

3 Results

Formatted: Heading 1

3.1 Characterization of MSI maps

The measurement areas ranged from 14907 to 26937 laser shots for each 5-cm ~~piece~~ slice (20957 ~~+-~~ ± 4134 =1σ), and thus ~40 shots per 100-µm horizon. On average, at 62% of the shots, at least one of the three compounds was detected. Pyropheophorbide *α* was detected in 61% of the spectra, while at least one alkenone was detected in 46.~~%~~ ~~and b~~Both alkenones were detected simultaneously in 34% of the spectra, which could then form swUk estimates (spotwise-calculated $U^{K'}_{37}$). When aggregating 200-µm horizons to time series, these detection rates amounted to~~, an average of~~ ~37 shots on average ~~per horizon~~that yielded at least one alkenone compound~~,~~ and an average of ~31 ~~yielded both~~simultaneous detections per horizon (see t~~T~~able 1 and S5 of the supplementary material).

We first investigated the replicability and signal content of individual MSI maps in terms of the similarity of their overall swUk (spotwise-calculated $U^{K'}_{37}$) values and distributions. The ~~maps of~~ swUk value maps~~s~~ showed strong spatial heterogeneity (Fig.~~ure~~ ~~2A~~2B). Despite this, the average values were highly consistent between MSI replicates: the standard error of the~~averaging~~ mean swUk~~s~~ per triplicate was just 0.001, corresponding to ~0.03°C (Prahl et al., 1987). Similarly, the level of spatial variability was consistent across the replicates. The average swUk variance within maps ('field variance') was 0.00595 ± 0.00004, corresponding to 2.34 ± 0.19 °C. The swUk distributions were similar across depth intervals and were unaffected by sediment structure (~~see~~ Fig. 2C).

Values from the same horizon can be aggregated into a single data ~~-~~point, and thereby, a time series can be constructed. The average variance of swU~~K~~k (spotwise $U^{K'}_{37}$) in these 200 µm horizons was similar to the observed total field variances: 0.006 ± 0.00005 (2.35 ± 0.21°C, supplementary material S4). Visual comparison between replicate time-series showed~~s~~ good agreement in terms of mean values and slow variation (see Fig. 2~~, panel~~ D) yet weak correlation of the fastest resolution of 200-µm steps, with an average Pearson's r of 0.12 and average RMSE of 0.03 (~0.89°C). Such weak correlations ~~is~~ most likely result from~~due to~~ a lack of fine-scale depth alignment.

Table 1: Map statistics averaged across replicates per depth interval. For "swUk mean" spotwise-calculated $U^{K'}_{37}$ values have been averaged for the replicate maps and subsequently per 5-cm depth interval. Accordingly, swUk variance is the average variance of swUk values ("field variance") of the replicate maps per depth interval. $U^{K'}_{37}$ units have been rounded to three digits, S.E. below 0.001 (~0.03°C) are not shown.

Depth (cm)	swUk mean	swUk variance	Number of spots	Coverage [%] (any compound)	Coverage [%] (both alkenones)	Coverage [%] (any alkenone)
0-5	0.523 ± 0.001	0.006	14907 ± 358	49.3 ± 1.1	31.5 ± 0.7	39.8 ± 0.9
5-10	0.529	0.006	26937 ± 563	62.3 ± 0.7	38.8 ± 0.5	49.6 ± 0.6
10-15	0.538	0.006	20002 ± 353	35.4 ± 0.9	20.5 ± 0.8	27.6 ± 0.9
15-20	0.534 ± 0.001	0.006	22043 ± 1788	68.4 ± 2.1	29 ± 2.9	43.5 ± 2.6
20-25	0.534 ± 0.001	0.006	18582 ± 1081	79.2 ± 4.5	42.9 ± 2.5	59.5 ± 3.4
25-30	0.528 ± 0.001	0.006	23269 ± 559	79.6 ± 1.2	40.1 ± 2.9	54.9 ± 2.5

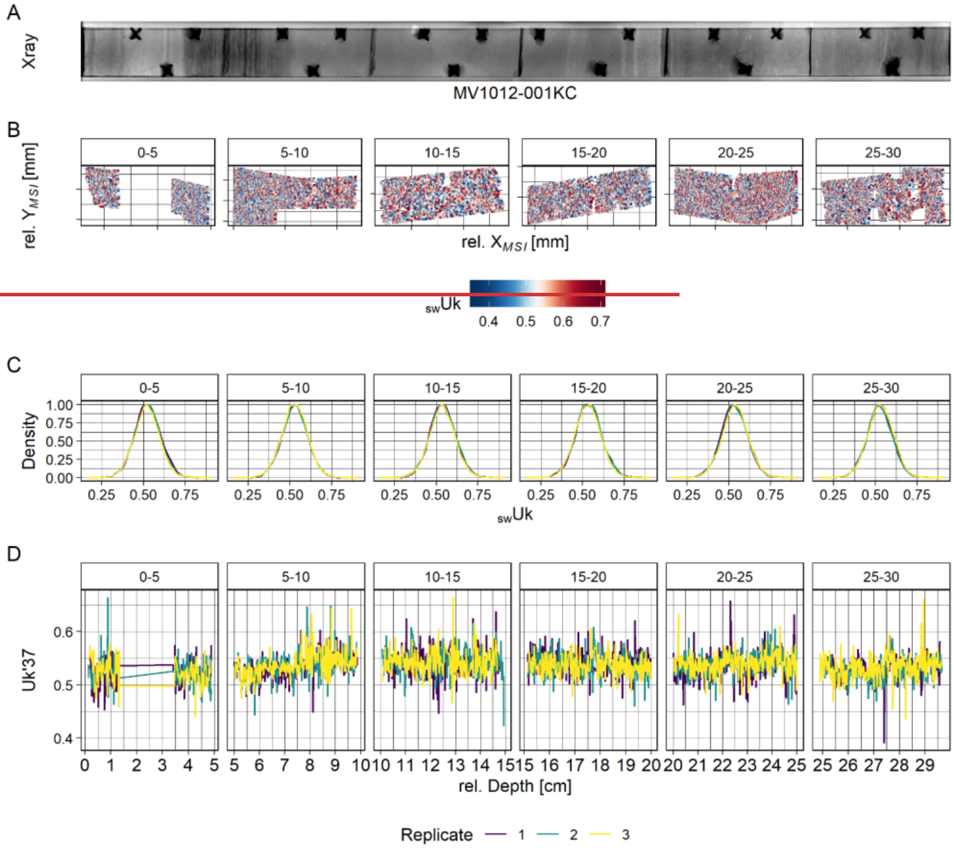

~~**Figure 2: Maps and time-series of the sediment section KC1. (A) X-ray density map, (B) exemplary swUk (spotwise $U^{K'}_{37}$) maps of one replicate per depth interval. Maps are shown as measured, on the MSI coordinate grid, before affine transformation onto Xray coordinates, values below 1% and above 99% quantiles were removed for optimal color scaling during plotting. (C) Scaled density plots of the spatial swUk maps per replicate, and (D) the resulting $U^{K'}_{37}$ time-series per replicate and depth interval. Note that the area corresponding to the 1761 AD floodlayer in depth interval 0-5 cm was removed prior to analyses.**~~

Formatted: Caption

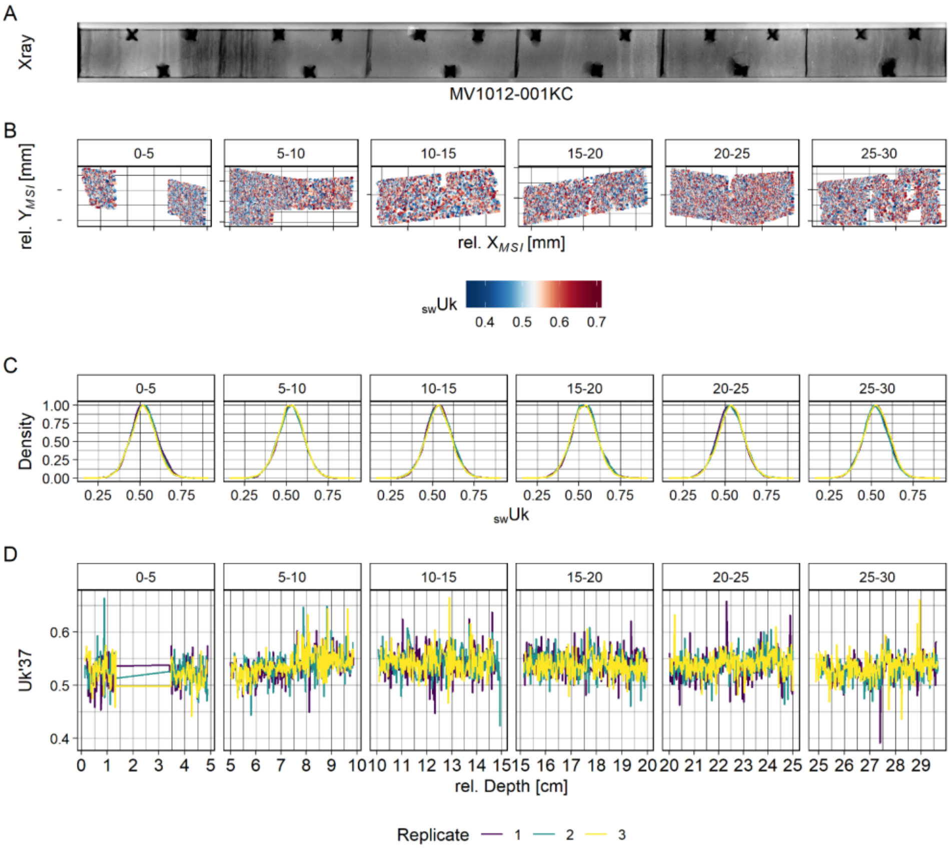

Figure 2: Maps and time-series of the sediment section KC1. (A) X-ray density map with black crosses or rectangles where material was removed as markers for orientation of the samples, (B) exemplary swUk (spotwise $U^{K'}_{37}$) maps of one replicate per depth interval. Maps are shown on the MSI coordinate grid before affine transformation onto X-ray coordinates. swUk values below the 1% and above the 99% quantiles were removed for improved color scaling during plotting. (C) Scaled density plots of the spatial swUk maps per replicate, and (D) the resulting $U^{K'}_{37}$ time-series per

Formatted: Font: Bold

Formatted: Font: Bold

Formatted: Font: Bold

Formatted: Font: Bold

Formatted: Font: Bold

replicate and depth interval. Note that the area corresponding to the 1761 AD floodlayer in depth interval 0-5 cm was removed prior to analyses. For A, B and D the directionality is from left ("modern") to right ("past"). Note that an exposure artefact was removed from the X-ray photography of KC1 at ~20-25 cm. An unaltered version can be found in Supplementary Fig. S4.

3.2 Microscale Analyses of Spatial Heterogeneity

Formatted: Heading 2

After confirming consistency between replicates on a~~the~~ coarse~~r,~~ whole-slice level, we examined the spatial proxy heterogeneity using maps of spotwise-calculated Uk'$_{37}$ values (swUk). These spatial patterns showed high variability both across depth and laterally, with average swUk variances across depths and horizons both approximating 0.00596 (vertical, ~~vertical~~downcore: 0.00597; horizontal~~tal~~: 0.00596). To explore the structure of this heterogeneity in more detail, we focused on two representative depths~~—~~, one laminated and one mixed, ~~—~~along with their respective replicates (Fig. ~~2~~3). Notably, the clear laminations ~~seen~~ observed in the X-ray scans (e.g., at 5–7 cm; Fig. 2A, top row) are not reflected in the swUk patterns. Instead, both laminated and mixed intervals show swUk values forming small clusters of neighboring pixels with similar temperatures.

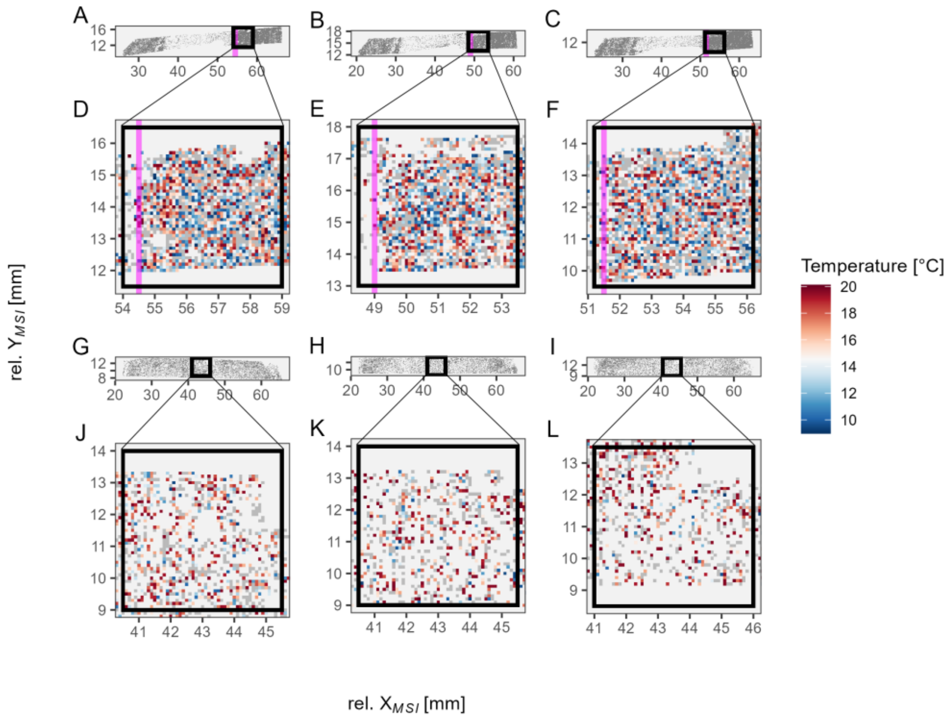

Figure 3: Overview maps of the measurement areas for three replicates from 0-5 cm (A-C) and 10 -15 cm (G-I) depth: gray areas indicate spots in which alkenones were successfully detected. Downcore direction is from left to right, y axes correspond to layers parallel to the sediment surface. Pink line: onset of the 1761AD flood layer; black rectangles indicate 5x5mm inlets as shown in D-F and J-L. These zoom-ins show values for swUk (spotwise $U_{37}^{K'}$) converted to SST (Prahl and Wakeham, 1987). D-F represent a laminated interval below the flood layer, while J-L correspond to a thoroughly mixed interval of KC1 ("olive turbidite", event 1D in Hendy et al. (2013)). Maps are shown as measured, before affine transformation onto Xray coordinates.

Formatted: Font: Bold

Formatted: Font: Bold

Formatted: Font: Bold

Formatted: Font: Bold

Formatted: Font: Bold

Formatted: Font: Bold

Formatted: Font: Bold

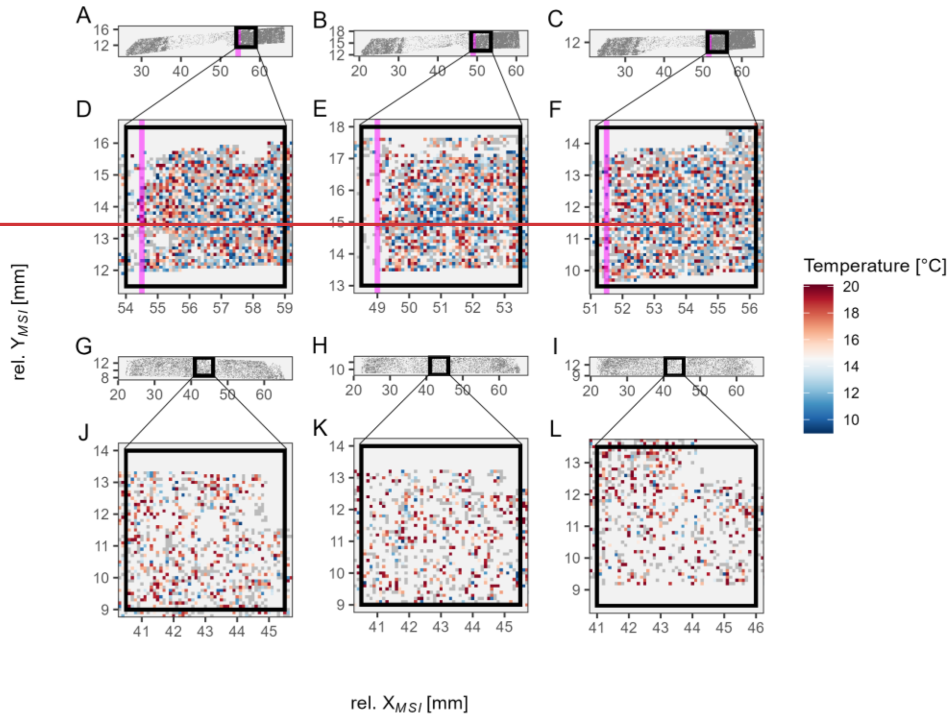

~~**Figure 3: Overview maps of the measurement areas for three replicates from 0-5 cm (A-C) and 10 -15 cm (G-I) depth: gray areas indicate spots in which alkenones were successfully detected. Pink line: onset of the 1761AD flood layer; black rectangles indicate 5x5mm inlets as shown in D-F and J-L. These zoom-ins show values for swUk (spotwise $U^{K'}_{37}$) converted to SST (Prahl and Wakeham, 1987). D-F represent a laminated interval below the flood layer, while J-L correspond to a thoroughly mixed interval of KC1B (“olive turbidite”, event 1D in Hendy et al. (2013)). Maps are shown as measured, before affine transformation onto Xray coordinates.**~~

~~*Table 1: Map statistics averaged across replicates per depth interval. For “swUk mean” spotwise-calculated $U^{K'}_{37}$ values have been averaged for the replicate maps and subsequently per 5-cm depth interval. Accordingly, swUk variance is the average variance of swUk values (“field variance”) of the replicate maps per depth interval. $U^{K'}_{37}$ units have been rounded to three digits, S.E. below 0.001 (~ 0.03°C) are not shown.*~~

~~Depth (cm)~~	~~swUk mean~~	~~swUk variance~~	~~Number of spots~~	~~Coverage [%] (any compound)~~	~~Coverage [%] (both alkenones)~~	~~Coverage [%] (any alkenone)~~
~~0-5~~	~~0.523 ± 0.001~~	~~0.006~~	~~14907 ± 358~~	~~49.3 ± 1.1~~	~~31.5 ± 0.7~~	~~39.8 ± 0.9~~
~~5-10~~	~~0.529~~	~~0.006~~	~~26937 ± 563~~	~~62.3 ± 0.7~~	~~38.8 ± 0.5~~	~~49.6 ± 0.6~~
~~10-15~~	~~0.538~~	~~0.006~~	~~20002 ± 353~~	~~35.4 ± 0.9~~	~~20.5 ± 0.8~~	~~27.6 ± 0.9~~
~~15-20~~	~~0.534 ± 0.001~~	~~0.006~~	~~22043 ± 1788~~	~~68.4 ± 2.1~~	~~29 ± 2.9~~	~~43.5 ± 2.6~~
~~20-25~~	~~0.534 ± 0.001~~	~~0.006~~	~~18582 ± 1081~~	~~79.2 ± 4.5~~	~~42.9 ± 2.5~~	~~59.5 ± 3.4~~
~~25-30~~	~~0.528 ± 0.001~~	~~0.006~~	~~23269 ± 559~~	~~79.6 ± 1.2~~	~~40.1 ± 2.9~~	~~54.9 ± 2.5~~

To describe local (dis) similarities in biomarker patterns more precisely,~~In order to more precisely describe local (dis)similarities in biomarker patterns,~~ we obtained averaged variogram estimates of compounds and swUk~~.~~. This approach revealed~~s~~ that only a small portion of total variability is spatially structured (Table 2) in KC1. The total map-level variance, the “sill” in the variograms, was~~is~~ 0.00595 (~2.34 °C), of which just 0.0002 (~0.43 °C) showed~~s~~ small-scale spatial structure, that is~~ i.e.,~~ clustering or increased similarity among neighboring values. Most of the variability (~93–99%, avg. 96%) is unstructured or unresolved, termed the nugget effect (C_0). A ~~H~~high contribution of C_0 can ~~point to~~ indicate variation, which is either spatially unresolved or intrinsic varia~~n~~bility~~ce~~ of the proxy~~,~~ or measurement noise. In contrast, pyropheophorbide α showed~~s~~ a slower decay of similarity with distance and a lower C_0 “nugget” component (80–96%, avg. ~86%), indicating stronger spatial structure~~ and a slower decay of similarity with distance~~ (Fig. 4 A, C green lines~~A~~).

We then separated vertical ~~-~~from horizontal similarity to distinguish between variability across successive depositional layers (in situ vertical, downcore) and within the same horizon (horizontal). It is important to note that the spatial plots in Fig. 2B and Fig. 3 are rotated by 90° to align with time-series convention, therefore variograms estimated over the vertical downcore direction in the original sediment position would have to be visualized left to right on these plots. As a proof of concept, we also applied this approach to a varved interval from a box core as ~~a~~ the best-case reference without sediment mixing (Alfken et al., 2020, 2021). In both sample sets, this separation (solid lines: original sediment position vertical, downcore; dashed: horizontal, Fig~~s~~. 4) reveals geometric anisotropy: similarity decreases more slowly in the horizontal than in the vertical direction~~s~~. This can be interpreted as the within-horizon variability, parallel to the sediment surface,~~nce~~ (dashed) being lower

Formatted: Subscript

Formatted: Subscript

and increasing more gradually with distance than between layers (solid). This pattern is most clearly visible in the ~~abundance~~ intensity data of pyrophophorbide α, but is also still detectable in the $C_{37:3}$ alkenone and $U^{K'}_{37}$ data. As expected, the differences ~~are~~ were clearer in the varved section of SBX than in the combined core KC1. Notably, in the varved section, pyropheophorbide α and, to a lesser extent, $U^{K'}_{37}$ show a sinusoidal pattern in ~~similarity~~ γ with peaks and troughs aligning with the annual sedimentation rate of ~1.4 mm (Thunell, 1998).~~,~~ ~~v~~Variograms of individual sediment ~~pieces~~ slices can be found in the supplements (~~S4~~S6).

Formatted: Subscript

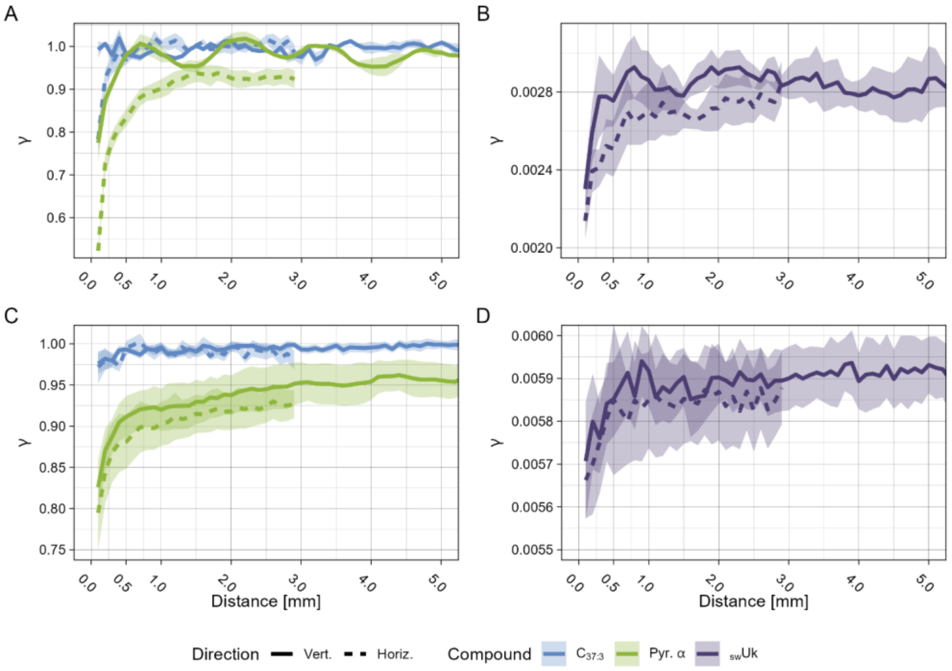

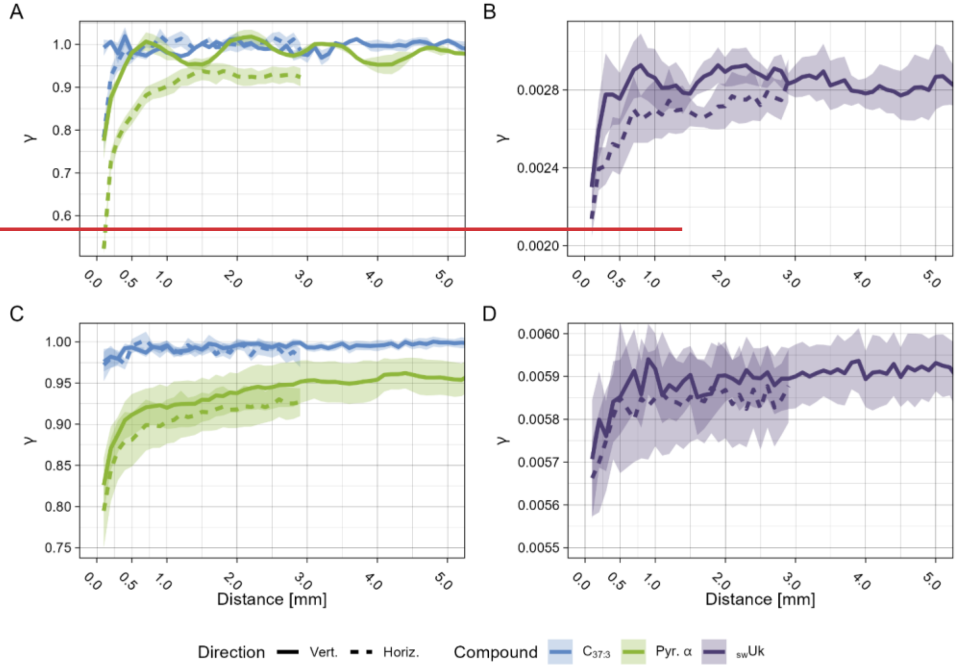

~~Figure 4: Variogram estimates of pyropheophorbide α and C37:3 intensities and swUk (spotwise $U^{K'}_{37}$) temperatures, showing the average variability of pairwise spot comparisons (γ) as a function of distance. A and B are obtained for the exemplary varved section of SBX, averaged over 3 replicates. C and D for sediment segment KC1, averaged over all replicates and depth intervals (3x 6x 5cm). Note that each panel has individual y-axes, as pyropheophorbide α and C37:3 values in A, C were scaled prior to calculation and are not in their native units, whereas in B, D γ values correspond to $U^{K'}_{37}$ units.~~

~~Table 2: Estimated swUk variogram parameters averaged per piece.~~

~~Depth [rel.cm]~~	~~Sill (total field variance)~~	~~Variance without spatial structuring (C0)~~	~~Variance with spatial structuring~~	~~C0 contribution to total variance [%]~~
~~0-5~~	~~0.005871~~	~~0.005467~~	~~0.000404~~	~~93.12~~

~~5-10~~	~~0.005878~~	~~0.005595~~	~~0.000284~~	~~95.19~~
~~10-15~~	~~0.005946~~	~~0.005883~~	~~6.32E-05~~	~~98.94~~
~~15-20~~	~~0.006121~~	~~0.006038~~	~~8.32E-05~~	~~98.62~~
~~20-25~~	~~0.006094~~	~~0.005934~~	~~0.00016~~	~~97.39~~
~~25-30~~	~~0.00582~~	~~0.005612~~	~~0.000208~~	~~96.42~~

Figure 4: Variogram estimates of pyropheophorbide α and C37:3 intensities and swUk (spotwise $U^{K'}_{37}$) temperatures, showing the average variability of pairwise spot comparisons (γ) as a function of distance. Solid lines indicate sample variogram estimates along the vertical, downcore direction of the original sediment position; dashed lines indicate within-layer estimates, parallel to the sediment surface. A and B are obtained for the exemplary varved section of SBX, averaged over 3 replicates. C and D for sediment segment KC1, averaged over all replicates and depth intervals (3x 6x 5cm). Note that each panel has individual y-axes, as pyropheophorbide α and C37:3 values in A, C were scaled prior to calculation and are not in their native units, whereas in B, D γ values correspond to $U^{K'}_{37}$ units.

Formatted: Font: Bold

Formatted: Font: Bold

Formatted: Font: Bold

Formatted: Font: Bold

Formatted: Font: Bold

Table 2: Estimated swUk variogram parameters averaged per 5 cm depth interval (piece).

Depth [rel.cm]	Sill (total field variance)	Variance without spatial structuring (C_0)	Variance with spatial structuring	C_0 contribution to total variance [%]
0-5	0.005871	0.005467	0.000404	93.12
5-10	0.005878	0.005595	0.000284	95.19
10-15	0.005946	0.005883	6.32E-05	98.94
15-20	0.006121	0.006038	8.32E-05	98.62
20-25	0.006094	0.005934	0.00016	97.39
25-30	0.00582	0.005612	0.000208	96.42

3.3 Frequency-dependent Signal and Noise Components of Replicated Time-Series

Formatted: Heading 2

Replication within 5-cm depth intervals allowed us to quantify the reproducibility between individual MSI slices and estimate the SNR of the resulting time series. The frequency-dependent separation of the shared signal and independent noise shows that the replicates contain increasing signal content with timescale and flat noise spectra. Signal spectra showed an average slope of ~-1.7 ~~on average~~ estimated between f=1/10 mm^{-1} and f=1/2 mm^{-1}, the interval of the spectral estimates not affected by bias and gaps. The noise components showed no frequency dependency (~-0.13 between f=1/10 mm^{-1} and f=1/2 mm^{-1}, see Fig. 5A).

As a reference, we added noise spectra derived from total field variance (black dotted line, Fig. 5A), downscaled by a factor of ~37~~,~~ — the average number of swUk measurements per horizon at 200 µm resolution (see also Table 2)~~,~~ — to illustrate how independent (measurement) noise scales with averaging. The actual noise level was ~13 higher than this baseline, indicating a noise reduction weaker than 1/n when aggregating to horizonwise $\mathrm{U}_{37}^{\mathrm{K}'}$ data.

Integrating the spectra from high to low frequencies yields the integrated SNR ($iSNR$), which is an estimate of the expected SNR at a given sampling resolution. $iSNR$ values reach from ~0.24-~3.1, considering sampling from submillimeter to centimeter steps (Fig. 5B).

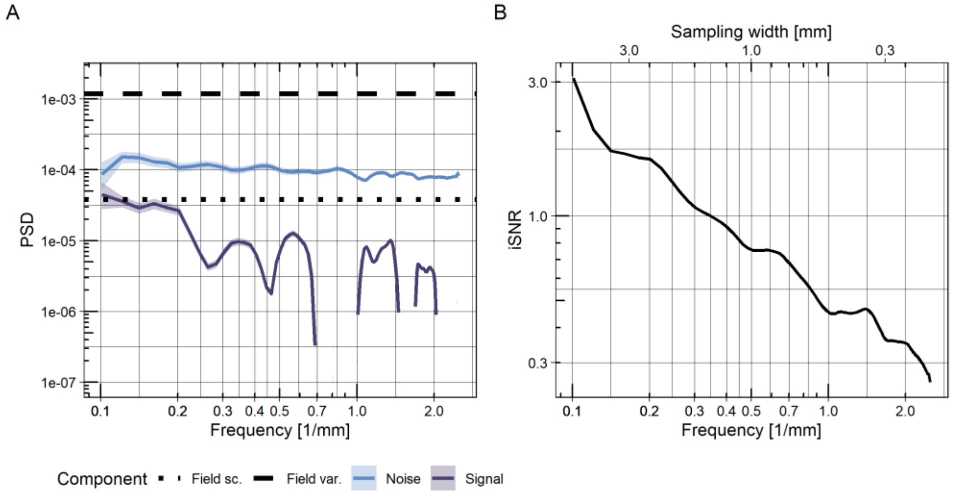
A
B
PSD
1e-03
1e-04
1e-05
1e-06
1e-07
0.1
0.2
0.3
0.4
0.5
0.7
1.0
2.0
Frequency [1/mm]
Sampling width [mm]
3.0
1.0
0.3
iSNR
3.0
1.0
0.3
0.1
0.2
0.3
0.4
0.5
0.7
1.0
2.0
Frequency [1/mm]
Component
Field sc.
Field var.
Noise
Signal

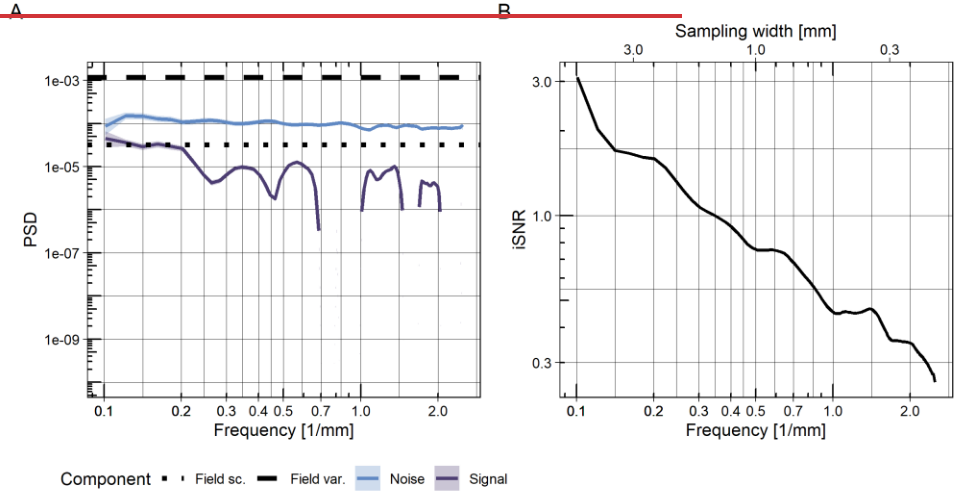
A
B
PSD
1e-03
1e-05
1e-07
1e-09
0.1
0.2
0.3
0.4
0.5
0.7
1.0
2.0
Frequency [1/mm]
Sampling width [mm]
3.0
1.0
0.3
iSNR
3.0
1.0
0.3
0.1
0.2
0.3
0.4
0.5
0.7
1.0
2.0
Frequency [1/mm]
Component
Field sc.
Field var.
Noise
Signal

Figure 5: Frequency dependent Signal and noise components in comparison to field variance (A) and the resulting integrated SNR (iSNR) estimate (B). Dashed line shows the average variance of the swUk field in black; the dotted line is the field variance downscaled by the average number of swUk shots per horizon, imitating the noise reduction during time series processing.

~~**Figure 5:** Frequency dependent Signal and noise components in comparison to field variance (A) and the resulting integrated SNR (iSNR) estimate (B). Dashed line shows the average variance of the swUk field in black; the dotted line is the field variance downscaled by the average number of swUk shots per horizon, imitating the noise reduction during time series processing.~~

Formatted: Font: Bold

We then assessed the influence of sediment structure on time-~~-~~domain signal-to-noise variance ratios (Fisher et al., 1985) (~~i.e.~~that is SNR between the variance of the noise and signal components) of the different depth intervals in comparison to the "best case" varved 5 cm section published earlier (Alfken et al., 2020, 2021). We also repeated the analysis using different aggregation steps (Fig. 6) to assess the impact of data processing choices. The tested sampling widths ranged from 200 to 1400 µm, which, under ideal preservation and an average sedimentation rate of 1.4 mm/yr (Thunell, 1998), would correspond to monthly to annual resolution. For core segment KC1, these SNRs ranged from ~0 in the most strongly mixed interval to ~2 in an interval with partially preserved varves (Fig. 6). In comparison, the varved section of SBX reached SNRs of ~2.8 on average.

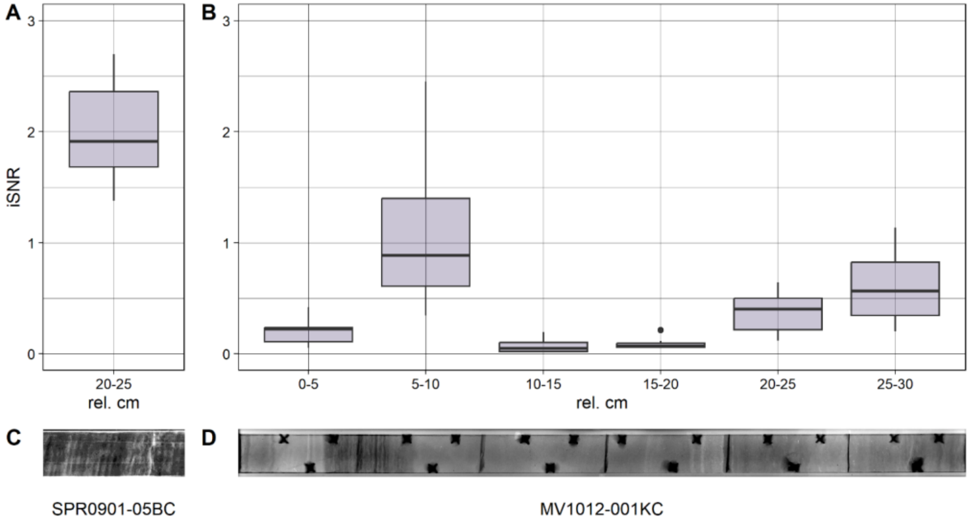

Figure 6: Comparison of sediment structure and SNR based on time domain signal-to-noise variance ratios (Fisher et al., 1985), resulting from aggregating horizons from 0.2 to 1.4mm, the theoretical maximum aggregation for annual resolution (Thunell et al 1995). A and C show a 5 cm exemplary interval from the varved upper part of SBB (ca. 1913-1935). C and D show the KC1 segment which represents the different conditions found at SBB throughout the late Holocene, ranging from laminated sediments, varying degrees of mixing to turbidites. Note that the 1761AD flood layer in KC1 0 – 5 cm was removed from the timeseries prior to SNR estimation. C and D are X-ray density maps of the respective samples, brighter colors indicate denser material. The black holes are markers for orientation during sampling and to correct for distortion. Note that an exposure artefact was removed from the X-ray photography of KC1 at ~20-25 cm. An unaltered version can be found in Supplementary Fig. S4.

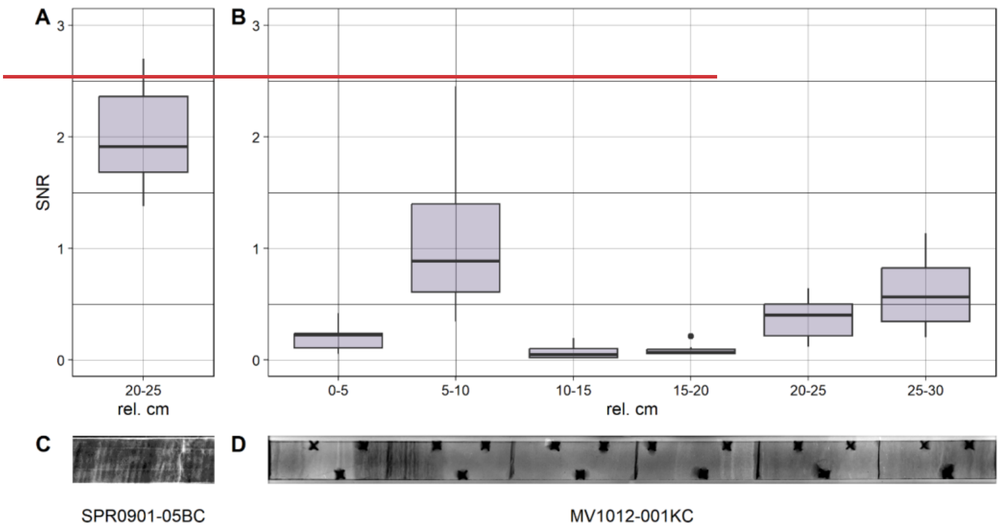

~~**Figure 6: Comparison of sediment structure and SNR based on time domain signal-to-noise variance ratios (Fisher et al., 1985), resulting from aggregating horizons from 0.2 to 1.4mm, the theoretical maximum aggregation for annual resolution (Thunell et al 1995). A and C show a 5 cm exemplary interval from the varved upper part of SBB (ca. 1913-1935). C and D show the KC1 segment which represents the different conditions found at SBB throughout the late Holocene, ranging from laminated sediments, varying degrees of mixing to turbidites. Note that the 1761AD flood layer in KC1 0 – 5 cm was removed from the timeseries prior to SNR estimation. C and D are X-ray density maps of the respective samples, brighter colors indicate denser material. The black holes are**~~

Formatted: Font: Bold

Formatted: Font: Bold

Formatted: Font: Bold

Formatted: Heading 1

~~**markers for orientation during sampling and to correct for distortion. Note that an exposure artefact was removed from the X-ray photography of KC1 at ~20-25 cm. An unaltered version can be found in Supplementary Fig. S3.**~~

4 Discussion

This study investigated the spatial heterogeneity of biomarkers at submillimeter resolutions and its effect on the time-scale-dependent signal-to-noise ratios of MSI-based high-resolution SST reconstructions. In the following sections, we discuss the observed spatial heterogeneity of biomarkers and the influence of sediment mixing intensity on the interpretability of high-resolution SST reconstructions.

4.1. Spatial Heterogeneity of Biomarkers

Formatted: Heading 2

Variogram analyses showed greater similarity across sedimentary horizons than downcore (see Fig. 4, dashed and solid lines), consistent with the expectation of layered archives, where variation over depth includes additional variability from changing climate signals over time (Fisher et al., 1985; Münch and Laepple, 2018).

Biomarker maps revealed sub-millimeter-scale clustering and marked differences in spatial heterogeneity between compounds (Fig. 4, 5). For swUk, the variance exhibiting~~showing~~ spatial structuring wa~~i~~s minimal (~4%). Under favorable sediment preservation conditions, varved sections manifest as oscillations in the variogram (Fig. 4 A, green solid lines and B purple solid lines), with wavelengths approximating the average sedimentation rate (Thunell, 1998).~~.~~

The high proportion of unstructured variance in our biomarker and proxy maps suggests significant noise at the individual spot level. Aggregating data across horizons enhances the signal content because noise is largely uncorrelated between spots at the microscale. However, the study's data does not allow us to determine whether this noise stems from measurement errors or from the deposition of heterogeneous biomarker signals. ~~On one hand, s~~Strong shot-to-shot variation is a common issue in MSI (Tobias and Hummon, 2020). However, classic bulk sediment $U^{K'}_{37}$ estimates reflect averaged or smoothed signals, and it is difficult to estimate potentially contained~~the~~ heterogeneity.~~ they are capturing.~~ For example, water column and sediment trap data display a broader range of $U^{K'}_{37}$ values around ~~the~~ measured ocean temperatures than core tops, and laboratory cultures have been shown to exhibit even greater variability in biomarker ratios than observations in natural settings (Conte et al., 1995; Conte and Eglinton, 1993; Freeman and Wakeham, 1992; Herbert et al., 1998; Sikes and Volkman, 1993). Our observed proxy spot-level variance is smaller than that of the monthly SST estimates for SBB, yet larger than the interannual variation (see supp. S7~~5~~), suggesting that the observed heterogeneity may indeed originate from SST and capture variability typically lost~~ in~~ in bulk sediment samples. ~~Therefore,~~ MSI-based $U^{K'}_{37}$ maps ~~can~~ could help ~~reconcile~~ to bridge the steps along the proxy formation chain and potentially provide high-frequency climate variability information similar to the developments in foraminifera isotope proxies with the utilization of individual foraminiferal analyses in contrast to bulk data (Glaubke et al., 2021). ~~.~~

The small-scale clustering (~0.5 mm) observed in the biomarker maps impliies~~y~~ that, for optimal sampling, MSI measurement windows should be in the range of a few millimeters to be wide enough to 1) have enough successful shots to overcome sparse detections, and 2) avoid bias or correlated noise that could arise from only targeting single proxy clusters. Therefore, the typical measurement window widths of ~4-8 mm used in this and earlier studies (Alfken et al., 2020, 2021; Liu et al., 2022; Napier et al., 2022; Obreht et al., 2022a; Wörmer et al., 2014, 2022) should effectively reduce the noise in downcore records.

4.2. Timescale dependent signal to noise estimations

Formatted: Heading 2

Averaging across a diverse range of sediment preservation conditions in core segment KC1, we detected iSNRs around ~1 at interannual resolution, increasing to 3 at subdecadal (ENSO) resolution. The extracted noise component shows no dependence on time scale, whereas~~ile~~ the variance of the signal components increases with time scale. This suggests that temporal aggregation effectively reduces noise in individual time series and enhances the relative potential climate signal content. Additionally, stacking multiple replicates would further decrease the noise contribution by a factor of 1/~~N~~*n*, boosting the relative signal content.

The iSNR >> 1 indicates that individual MSI series are representative of their core samples and demonstrate potential for high-resolution climate reconstructions~~,~~ at subdecadal resolution in the case of the SBB sedimentary archive containing laminated and mixed intervals. This aligns with findings from O'Mara et al. (2019), who estimated the effective temporal resolution of neighboring laminated SST records from San Lazaro Basin to approximately decadal without replication or stacking.

Commented [JV1]: Extend on SNR>1/ still use coarser

One limitation of our method is its sensitivity to depth misalignment between replicates, which could lead to a bias in SNR estimates at the fastest temporal and corresponding spatial scales («1 mm). To minimize these effects, we used sediment marker holes and the mapped~~ing~~ ~~of~~ the MSI data onto X-ray imagery. More advanced image correction and alignment ~~might~~ may further reduce these biases in the future. However, low SNRs at <<1 mm also match expectations based on reports by Bernhard et al. (~~Bernhard et al.,~~ 2003), who documented living microorganisms such as ciliates, foraminifera, and bacterial colonies growing under severe oxygen limitation, even within otherwise undisturbed laminae, pointing to an alternative cause~~source~~ for the low SNRs at the fastest resolutions.

The current SNR estimates are based on closely spaced samples (~~sequential 100 µm~~ cryotome cuts within <1 mm horizontal distance) to provide as identical conditions as possible under natural conditions to estimate the baseline noise level for individual MSI-derived Uk'37 time series. This leads to the tradeoff that spatially correlated noise between adjacent cuts may also be interpreted as a shared signal, effectively barring the direct interpretation of the derived SNRs in terms of pure climatic signal. However, the correlation of ~0.6 between MSI-derived Uk'37 time series and in situ 0 – 30 m water column temperatures reported by Alfken et al. (~~Alfken et al.,~~ 2020) is close to the upper achievable limit ~0.77 as suggested by our SNR estimates for the exemplary varved pieces (Fig. 6 A and S3). Together with the shortrange spatial similarity found in the

Formatted: Not Highlight

variogram analyses (Fig. 4) we therefore expect correlated noise between replicates to play a minor role. ~~and therefore represent an upper bound for SNR, as spatially correlated noise between adjacent cuts may also be interpreted as a climate signal. (Alfken et al., 2020)Further, the 5-cm sample length imposed by the workflow restricts the estimation of SNRs to less than cm scales.~~ Future studies using samples at larger lateral spatial scales (e.g., nearby sediment cores) ~~and~~ combined with longer core segments will help to better characterize and separate the spatial structure of signal and~~the~~ noise components.

4.3 The influence of lamina preservation

Formatted: Heading 2

Variogram analyses demonstrated that the degree to which a spatial structure is preserved in the sedimentary archive strongly influences the spatial variation patterns of the biomarkers ~~(see supplements Fig. S4)~~. Under strong mixing conditions, such as olive turbidite 1D ~1738 AD (Hendy et al., 2013), horizontal variation and variation over depth are similar. However, as lamina preservation increases, the anisotropy of the variograms becomes more pronounced, with longer ranges of similarity within horizons and generally greater variation over depth, suggesting potential additional climate variation (see ~~supp.~~Supplements S6~~4~~). Additionally, the variogram of a varved example section from the early 20th century captures the rhythmic seasonal variation of the biomarkers over depth (Fig. 4 A green solid line), whereas this seasonal pattern is destroyed in the lower sediment sections.

Across a broad, yet plausible range of processing choices, the influence of sediment structure was the dominant factor affecting the high-~~–~~frequency replicability (SNR) between individual MSI time-series. The achieved SNRs at sub-~~m~~millimeter~~m~~ to interannual (~1.4 mm) sampling ~~follow~~ closely follow the degree of preservation of lamina, as visible in the X-ray (Fig. 6C, D). Earlier studies ~~showed~~ have shown that the mixing and bioturbation intensities assessed in this study are representative for the Holocene and late Pleistocene SBB sediments (Anderson et al., 1990; Behl, 1995) and are closely linked to warm phases, which might limit the potential of high-resolution MSI variability estimates to snapshots during favorable oceanic regimes.

5 Conclusion

Formatted: Heading 2

Recent methodological advances allow the measurement of biomarkers and sediment proxies with increasingly fine spatial resolution, significantly enhancing the potential for reconstructing high-resolution climate variability from the past, well beyond the scope of instrumental records. Our analysis of replicated MSI-based biomarker maps from a single Santa Barbara Basin core reveals how spatial variability reflects both the preservation state of the sediment and the fidelity of SST proxy signals. We show ~~that~~ that biomarkers in marine sediments display significant heterogeneity, even within uniformly deposited horizons and well-preserved laminae. This variability might serve as the missing link needed to reconcile the smooth bulk sediment SST estimates with the highly variable results from laboratory culture and water column studies. The degree of lamina preservation is the primary factor controlling proxy replicability. In laminated intervals, signal-to-noise ratios increase with temporal scale, reaching values suitable for subdecadal interpretations, even when using single MSI measurements. In contrast, mixed sediments show reduced signal content, particularly at higher frequencies, limiting the resolution of the interpretable variability.

To fully exploit the potential of MSI-based time series, further refinement of data processing methods is needed to minimize noise introduced during the conversion of spatial measurements to SST estimates. Regional replication is also essential ~~to isolate~~for isolating shared climate signals and suppressing locally correlated noise. With optimized workflows and stacking approaches, MSI-derived SST records from the Santa Barbara Basin show strong potential to resolve the range from interannual to centennial variability throughout the Holocene and Late Pleistocene, offering a powerful complement to existing paleoclimate archives.

Code Availability

The code for this study has been archived and is accessible under https://doi.org/10.5281/zenodo.17352962.

Data Availability

Data can be obtained via 10.5281/zenodo.18681999.

Formatted: Default Paragraph Font

Author contribution

Jannis Viola: Conceptualization, Data curation, Formal analysis, Investigation, Methodology, Visualization, Writing - Original Draft, Writing - Review & Editing, Validation, Project administration, Software; Lars Wörmer: Conceptualization, Methodology, Project administration, Resources, Writing - Review & Editing, Supervision, Validation; Kai-Uwe Hinrichs: Conceptualization, Funding acquisition, Resources, Supervision, Writing - Review & Editing; Thomas Laepple: Conceptualization, Funding acquisition, Methodology, Project administration, Supervision, Writing - Review & Editing, Validation;

Competing Interests

Formatted: Heading 1

The authors declare that they have no known competing financial interests or personal relationships that could have appeared to influence the work reported in this paper.

Acknowledgements

We thank the scientists, technicians and support staff of cruises MV1012 and SPR0901 for the retrieval of the core material and especially Richard Norris and Janina Groninga for sampling the cores at Scripps Institution of Oceanography's geological collection. Furthermore, we would like to thank Jenny Altun and Susanne Alfken for laboratory training and help during the measurements, as well as Weimin Liu for invaluable help during processing. LLMs have been used to improve flow of text, as well as to correct grammar and spelling.

Financial support

This project has received funding from the European Research Council (ERC) under the European Union's Horizon 2020 research and innovation programme (grant agreement no. 716092). Additionally, this research was supported by Germany's Excellence Strategy (EXC-2077) project 390741603 'The Ocean Floor – Earth's Uncharted Interface'.

References

Alfken, S., Wörmer, L., Lipp, J. S., Wendt, J., Taubner, H., Schimmelmann, A., and Hinrichs, K.-U.: Micrometer scale imaging of sedimentary climate archives – Sample preparation for combined elemental and lipid biomarker analysis, Organic Geochemistry, 127, 81–91, https://doi.org/10.1016/j.orggeochem.2018.11.002, 2019.

Alfken, S., Wörmer, L., Lipp, J. S., Wendt, J., Schimmelmann, A., and Hinrichs, K.: Mechanistic Insights Into Molecular Proxies Through Comparison of Subannually Resolved Sedimentary Records With Instrumental Water Column Data in the Santa Barbara Basin, Southern California, Paleoceanography and Paleoclimatology, 35, https://doi.org/10.1029/2020PA004076, 2020.

Alfken, S., Wörmer, L., Lipp, J. S., Napier, T., Elvert, M., Wendt, J., Schimmelmann, A., and Hinrichs, K.: Disrupted Coherence Between Upwelling Strength and Redox Conditions Reflects Source Water Change in Santa Barbara Basin During the 20th Century, Paleoceanog and Paleoclimatol, 36, e2021PA004354, https://doi.org/10.1029/2021PA004354, 2021.

Anderson, D. M.: Attenuation of millennial-scale events by bioturbation in marine sediments, Paleoceanography, 16, 352–357, https://doi.org/10.1029/2000PA000530, 2001.

Anderson, R. Y., Gardner, J. V., and Hemphill-Haley, E.: Variability of the Late Pleistocene-Early Holocene Oxygen-Minimum Zone off Northern California, in: Aspects of Climate Variability in the Pacific and the Western Americas, American Geophysical Union (AGU), 75–84, https://doi.org/10.1029/GM055p0075, 1989.

Anderson, R. Y., Linsley, B. K., and Gardner, J. V.: Expression of seasonal and ENSO forcing in climatic variability at lower than ENSO frequencies: evidence from Pleistocene marine varves off California, Palaeogeography, Palaeoclimatology, Palaeoecology, 78, 287–300, https://doi.org/10.1016/0031-0182(90)90218-V, 1990.

Ault, T. R., Deser, C., Newman, M., and Emile-Geay, J.: Characterizing decadal to centennial variability in the equatorial Pacific during the last millennium, Geophysical Research Letters, 40, 3450–3456, https://doi.org/10.1002/grl.50647, 2013.

Behl, R. J.: Sedimentary Facies and Sedimentology of the Late Quaternary Santa Barbara Basin, Site 893, Proceedings of the Ocean Drilling Program, 146/2, 295–308, https://doi.org/10.2973/odp.proc.sr.146-2.276.1995, 1995.

Bernhard, J. M., Visscher, P. T., and Bowser, S. S.: Submillimeter life positions of bacteria, protists, and metazoans in laminated sediments of the Santa Barbara Basin, Limnology and Oceanography, 48, 813–828, https://doi.org/10.4319/lo.2003.48.2.0813, 2003.

Blanchet, C. L., Tjallingii, R., Schleicher, A. M., Schouten, S., Frank, M., and Brauer, A.: Deoxygenation dynamics on the western Nile deep-sea fan during sapropel S1 from seasonal to millennial timescales, Climate of the Past, 17, 1025–1050, https://doi.org/10.5194/cp-17-1025-2021, 2021.

Bograd, S. J., Schroeder, I. D., and Jacox, M. G.: A water mass history of the Southern California current system, Geophys. Res. Lett., 46, 6690–6698, https://doi.org/10.1029/2019GL082685, 2019.

Bojinski, S., Verstraete, M., Peterson, T. C., Richter, C., Simmons, A., and Zemp, M.: The Concept of Essential Climate Variables in Support of Climate Research, Applications, and Policy, Bulletin of the American Meteorological Society, 95, 1431–1443, https://doi.org/10.1175/BAMS-D-13-00047.1, 2014.

Brassell, S. C., Eglinton, G., Marlowe, I. T., Pflaumann, U., and Sarnthein, M.: Molecular stratigraphy: a new tool for climatic assessment, Nature, 320, 129–133, https://doi.org/10.1038/320129a0, 1986.

Butz, C., Grosjean, M., Fischer, D., Wunderle, S., Tylmann, W., and Rein, B.: Hyperspectral imaging spectroscopy: a promising method for the biogeochemical analysis of lake sediments, JARS, 9, 096031, https://doi.org/10.1117/1.JRS.9.096031, 2015.

California State Department of Fish and Game; NOAA Fisheries; Scripps Institution of Oceanography: Chemical, physical, and other data collected in the coastal waters of California as part of the California Cooperative Fisheries Investigation (CalCOFI) project since 1949, 2001.

Chaler, R., Grimalt, J. O., Pelejero, C., and Calvo, E.: Sensitivity Effects in Uk‘37 Paleotemperature Estimation by Chemical Ionization Mass Spectrometry, Anal. Chem., 72, 5892–5897, https://doi.org/10.1021/ac001014q, 2000.

Chaler, R., Villanueva, J., and Grimalt, J. O.: Non-linear effects in the determination of paleotemperature *U*k′37 alkenone ratios by chemical ionization mass spectrometry, Journal of Chromatography A, 1012, 87–93, https://doi.org/10.1016/S0021-9673(03)01188-9, 2003.

Conte, M. H. and Eglinton, G.: Alkenone and alkenoate distributions within the euphotic zone of the eastern North Atlantic: correlation with production temperature, Deep Sea Research Part I: Oceanographic Research Papers, 40, 1935–1961, https://doi.org/10.1016/0967-0637(93)90040-A, 1993.

Conte, M. H., Thompson, A., Eglinton, G., and Green, J. C.: Lipid Biomarker Diversity in the Coccolithophorid Emiliania Huxleyi (prymnesiophyceae) and the Related Species Gephyrocapsa Oceanica1, Journal of Phycology, 31, 272–282, https://doi.org/10.1111/j.0022-3646.1995.00272.x, 1995.

Cressie, N. A. C.: Statistics for spatial data, Rev. ed., Wiley, New York, 900 pp., 1993.

Du, X., Hendy, I., and Schimmelmann, A.: A 9000-year flood history for Southern California: A revised stratigraphy of varved sediments in Santa Barbara Basin, Marine Geology, 397, 29–42, https://doi.org/10.1016/j.margeo.2017.11.014, 2018.

Fisher, D. A., Reeh, N., and Clausen, H. B.: Stratigraphic Noise in Time Series Derived from Ice Cores, Annals of Glaciology, 7, 76–83, https://doi.org/10.3189/S0260305500005942, 1985.

Freeman, K. H. and Wakeham, S. G.: Variations in the distributions and isotopic composition of alkenones in Black Sea particles and sediments, Organic Geochemistry, 19, 277–285, https://doi.org/10.1016/0146-6380(92)90043-W, 1992.

Glaubke, R. H., Thirumalai, K., Schmidt, M. W., and Hertzberg, J. E.: Discerning Changes in High-Frequency Climate Variability Using Geochemical Populations of Individual Foraminifera, Paleoceanography and Paleoclimatology, 36, e2020PA004065, https://doi.org/10.1029/2020PA004065, 2021.

Goericke, R., Strom, S. L., and Bell, M. A.: Distribution and sources of cyclic pheophorbides in the marine environment, Limnology and Oceanography, 45, 200–211, https://doi.org/10.4319/lo.2000.45.1.0200, 2000.

Gräler, B., Pebesma, E., and Heuvelink, G.: Spatio-Temporal Interpolation using gstat, The R Journal, 8, 204–218, 2016.

Hathorne, E., Dolman, A. M., and Laepple, T.: Assessing seasonal and inter-annual marine sediment climate proxy data, Paleoceanog and Paleoclimatol, e2023PA004649, https://doi.org/10.1029/2023PA004649, 2023.

Hendy, I. L., Dunn, L., Schimmelmann, A., and Pak, D. K.: Resolving varve and radiocarbon chronology differences during the last 2000 years in the Santa Barbara Basin sedimentary record, California, Quaternary International, 310, 155–168, https://doi.org/10.1016/j.quaint.2012.09.006, 2013.

Herbert, T. D., Schuffert, J. D., Thomas, D., Lange, C., Weinheimer, A., Peleo-Alampay, A., and Herguera, J.-C.: Depth and seasonality of alkenone production along the California Margin inferred from a core top transect, Paleoceanography, 13, 263–271, https://doi.org/10.1029/98PA00069, 1998.

Huang, B., Thorne, P. W., Banzon, V. F., Boyer, T., Chepurin, G., Lawrimore, J. H., Menne, M. J., Smith, T. M., Vose, R. S., and Zhang, H.-M.: Extended Reconstructed Sea Surface Temperature, Version 5 (ERSSTv5): Upgrades, Validations, and Intercomparisons, Journal of Climate, 30, 8179–8205, https://doi.org/10.1175/JCLI-D-16-0836.1, 2017.

Hülse, D., Vervoort, P., van de Velde, S. J., Kanzaki, Y., Boudreau, B., Arndt, S., Bottjer, D. J., Hoogakker, B., Kuderer, M., Middelburg, J. J., Volkenborn, N., Kirtland Turner, S., and Ridgwell, A.: Assessing the impact of bioturbation on sedimentary isotopic records through numerical models, Earth-Science Reviews, 234, 104213, https://doi.org/10.1016/j.earscirev.2022.104213, 2022.

Kirchner, J. W.: Aliasing in 1∕f^{α} noise spectra: Origins, consequences, and remedies, Phys. Rev. E, 71, 066110, https://doi.org/10.1103/PhysRevE.71.066110, 2005.

Laepple, T. and Huybers, P.: Global and regional variability in marine surface temperatures, Geophysical Research Letters, 41, 2528–2534, https://doi.org/10.1002/2014GL059345, 2014.

Li, C., Ding, S., Chen, M., Zhong, Z., Sun, Q., and Wang, Y.: Visualizing biogeochemical heterogeneity in soils and sediments: A review of advanced micro-scale sampling and imaging methods, Critical Reviews in Environmental Science and Technology, 53, 1229–1253, https://doi.org/10.1080/10643389.2022.2128239, 2023.

Liao, S., Liu, X.-L., Manz, K. E., Pennell, K. D., Novak, J., Santos, E., and Huang, Y.: Comprehensive analysis of alkenones by reversed-phase HPLC-MS with unprecedented selectivity, linearity and sensitivity, Talanta, 260, 124653, https://doi.org/10.1016/j.talanta.2023.124653, 2023.

Liu, H., Meyers, S. R., and Marcott, S. A.: Unmixing deep-sea paleoclimate records: A study on bioturbation effects through convolution and deconvolution, Earth and Planetary Science Letters, 564, 116883, https://doi.org/10.1016/j.epsl.2021.116883, 2021.

Liu, W., Alfken, S., Wörmer, L., Lipp, J. S., and Hinrichs, K.-U.: Hidden molecular clues in marine sediments revealed by untargeted mass spectrometry imaging, Front. Earth Sci., 10, 931157, https://doi.org/10.3389/feart.2022.931157, 2022.

Liu, W., JFViola, and Zander, Y.: weimin-liu/msiAlign: Release v20250407130502, , https://doi.org/10.5281/zenodo.15167672, 2025.

Maroufpoor, S., Bozorg-Haddad, O., and Chu, X.: Geostatistics, in: Handbook of Probabilistic Models, Elsevier, 229–242, https://doi.org/10.1016/B978-0-12-816514-0.00009-6, 2020.

McPartland, M. Y., Dolman, A. M., and Laepple, T.: Separating Common Signal From Proxy Noise in Tree Rings, Geophysical Research Letters, 51, e2024GL109282, https://doi.org/10.1029/2024GL109282, 2024.

Müller, P. J., Kirst, G., Ruhland, G., von Storch, I., and Rosell-Melé, A.: Calibration of the alkenone paleotemperature index U37K′ based on core-tops from the eastern South Atlantic and the global ocean (60°N-60°S), Geochimica et Cosmochimica Acta, 62, 1757–1772, https://doi.org/10.1016/S0016-7037(98)00097-0, 1998.

Münch, T. and Laepple, T.: What climate signal is contained in decadal- to centennial-scale isotope variations from Antarctic ice cores?, Climate of the Past, 14, 2053–2070, https://doi.org/10.5194/cp-14-2053-2018, 2018.

Münch, T., Kipfstuhl, S., Freitag, J., Meyer, H., and Laepple, T.: Regional climate signal vs. local noise: a two-dimensional view of water isotopes in Antarctic firn at Kohnen Station, Dronning Maud Land, Climate of the Past, 12, 1565–1581, https://doi.org/10.5194/cp-12-1565-2016, 2016.

Napier, T. J., Wörmer, L., Wendt, J., Lückge, A., Rohlfs, N., and Hinrichs, K.-U.: Sub-Annual to Interannual Arabian Sea Upwelling, Sea Surface Temperature, and Indian Monsoon Rainfall Reconstructed Using Congruent Micrometer-Scale Climate Proxies, Paleoceanography and Paleoclimatology, 37, e2021PA004355, https://doi.org/10.1029/2021PA004355, 2022.

Obreht, I., De Vleeschouwer, D., Wörmer, L., Kucera, M., Varma, D., Prange, M., Laepple, T., Wendt, J., Nandini-Weiss, S. D., Schulz, H., and Hinrichs, K.-U.: Last Interglacial decadal sea surface temperature variability in the eastern Mediterranean, Nat. Geosci., 15, 812–818, https://doi.org/10.1038/s41561-022-01016-y, 2022a.

Obreht, I., De Vleeschouwer, D., Wörmer, L., Kucera, M., Varma, D., Prange, M., Laepple, T., Wendt, J., Nandini-Weiss, S. D., Schulz, H., and Hinrichs, K.-U.: Last Interglacial decadal sea surface temperature variability in the eastern Mediterranean, Nat. Geosci., 15, 812–818, https://doi.org/10.1038/s41561-022-01016-y, 2022b.

O'Mara, N. A., Cheung, A. H., Kelly, C. S., Sandwick, S., Herbert, T. D., Russell, J. M., Abella-Gutiérrez, J., Dee, S. G., Swarzenski, P. W., and Herguera, J. C.: Subtropical Pacific Ocean Temperature Fluctuations in the Common Era: Multidecadal Variability and Its Relationship With Southwestern North American Megadroughts, Geophys. Res. Lett., 46, 14662–14673, https://doi.org/10.1029/2019GL084828, 2019.

Pebesma, E. J.: Multivariable geostatistics in S: the gstat package, Computers & Geosciences, 30, 683–691, https://doi.org/10.1016/j.cageo.2004.03.012, 2004.

Posit team: RStudio: Integrated Development Environment for R, Posit Software, PBC, Boston, MA, 2025.

Prahl, F. G. and Wakeham, S. G.: Calibration of unsaturation patterns in long-chain ketone compositions for palaeotemperature assessment, Nature, 330, 367–369, https://doi.org/10.1038/330367a0, 1987.

Prahl, F. G., Muehlhausen, L. A., and Zahnle, D. L.: Further evaluation of long-chain alkenones as indicators of paleoceanographic conditions, Geochimica et Cosmochimica Acta, 52, 2303–2310, https://doi.org/10.1016/0016-7037(88)90132-9, 1988.

R Core Team: R: A Language and Environment for Statistical Computing, R Foundation for Statistical Computing, Vienna, Austria, 2024.

Rama-Corredor, O., Cortina, A., Martrat, B., Lopez, J. F., and Grimalt, J. O.: Removal of bias in C37 alkenone-based sea surface temperature measurements by high-performance liquid chromatography fractionation, Journal of Chromatography A, 1567, 90–98, https://doi.org/10.1016/j.chroma.2018.07.004, 2018.

Reimers, C. E., Lange, C. B., Tabak, M., and Bernhard, J. M.: Seasonal spillover and varve formation in the Santa Barbara Basin, California, Limnology and Oceanography, 35, 1577–1585, https://doi.org/10.4319/lo.1990.35.7.1577, 1990.

Schiffelbein, P.: Effect of benthic mixing on the information content of deep-sea stratigraphical signals, Nature, 311, 651–653, https://doi.org/10.1038/311651a0, 1984.

Schimmelmann, A. and Lange, C. B.: Tales of 1001 varves: a review of Santa Barbara Basin sediment studies, Geological Society, London, Special Publications, 116, 121–141, https://doi.org/10.1144/GSL.SP.1996.116.01.12, 1996.

Schimmelmann, A., Lange, C. B., Berger, W. H., Simon, A., Burke, S. K., and Dunbar, R. B.: Extreme climatic conditions recorded in Santa Barbara Basin laminated sediments: the 1835–1840 Macoma event, Marine Geology, 106, 279–299, https://doi.org/10.1016/0025-3227(92)90134-4, 1992.

Schimmelmann, A., Lange, C. B., Schieber, J., Francus, P., Ojala, A. E. K., and Zolitschka, B.: Varves in marine sediments: A review, Earth-Science Reviews, 159, 215–246, https://doi.org/10.1016/j.earscirev.2016.04.009, 2016.

Sikes, E. L. and Volkman, J. K.: Calibration of alkenone unsaturation ratios (Uk'37) for paleotemperature estimation in cold polar waters, Geochimica et Cosmochimica Acta, 57, 1883–1889, https://doi.org/10.1016/0016-7037(93)90120-L, 1993.

Soutar, A. and Crill, P. A.: Sedimentation and climatic patterns in the Santa Barbara Basin during the 19th and 20th centuries, GSA Bulletin, 88, 1161–1172, https://doi.org/10.1130/0016-7606(1977)88%253C1161:SACPIT%253E2.0.CO;2, 1977.

Suigetsu 2006 Project Members and Nakagawa, T.: High-precision sampling of laminated sediments: Strategies from Lake Suigetsu, PAGES Mag, 22, 12–13, https://doi.org/10.22498/pages.22.1.12, 2014.

Szymczak-Żyła, M., Kowalewska, G., and Louda, J. W.: Chlorophyll-*a* and derivatives in recent sediments as indicators of productivity and depositional conditions, Marine Chemistry, 125, 39–48, https://doi.org/10.1016/j.marchem.2011.02.002, 2011.

Thomson, D. J.: Spectrum estimation and harmonic analysis, Proceedings of the IEEE, 70, 1055–1096, https://doi.org/10.1109/PROC.1982.12433, 1982.

Thunell, R. C.: Particle fluxes in a coastal upwelling zone: sediment trap results from Santa Barbara Basin, California, Deep Sea Research Part II: Topical Studies in Oceanography, 45, 1863–1884, https://doi.org/10.1016/S0967-0645(98)80020-9, 1998.

Thunell, R. C., Tappa, E., and Anderson, D. M.: Sediment fluxes and varve formation in Santa Barbara Basin, offshore California, Geology, 23, 1083–1086, https://doi.org/10.1130/0091-7613(1995)023%253C1083:SFAVFI%253E2.3.CO;2, 1995.

Tierney, J. E. and Tingley, M. P.: BAYSPLINE: A New Calibration for the Alkenone Paleothermometer, Paleoceanography and Paleoclimatology, 33, 281–301, https://doi.org/10.1002/2017PA003201, 2018.

Tobias, F. and Hummon, A. B.: Considerations for MALDI-Based Quantitative Mass Spectrometry Imaging Studies, J Proteome Res, 19, 3620–3630, https://doi.org/10.1021/acs.jproteome.0c00443, 2020.

Wikle, C. K., Zammit-Mangion, A., and Cressie, N. A. C.: Spatio-temporal statistics with R, CRC Press, Taylor & Francis Group, Boca Raton, 380 pp., 2019.

de Winter, N. J., Agterhuis, T., and Ziegler, M.: Optimizing sampling strategies in high-resolution paleoclimate records, Climate of the Past, 17, 1315–1340, https://doi.org/10.5194/cp-17-1315-2021, 2021.

Wörmer, L., Elvert, M., Fuchser, J., Lipp, J. S., Buttigieg, P. L., Zabel, M., and Hinrichs, K.-U.: Ultra-high-resolution paleoenvironmental records via direct laser-based analysis of lipid biomarkers in sediment core samples, Proceedings of the National Academy of Sciences, 111, 15669–15674, https://doi.org/10.1073/pnas.1405237111, 2014.

Wörmer, L., Wendt, J., Boehman, B., Haug, G. H., and Hinrichs, K.-U.: Deglacial increase of seasonal temperature variability in the tropical ocean, Nature, 612, 88–91, https://doi.org/10.1038/s41586-022-05350-4, 2022.

Zander, P. D., Wienhues, G., and Grosjean, M.: Scanning Hyperspectral Imaging for In Situ Biogeochemical Analysis of Lake Sediment Cores: Review of Recent Developments, J Imaging, 8, 58, https://doi.org/10.3390/jimaging8030058, 2022.

Zander, Y., Liu, W., Viola, J., Altun, J., Groninga, J., Nettersheim, B., Kapiri, M.-S., Obreht, I., and Wörmer, L.: Mass spectrometry imaging in the earth sciences - A tutorial to the micrometer-scale mapping of molecular fossils via MALDI FT-ICR MS, Analytica Chimica Acta, 345142, https://doi.org/10.1016/j.aca.2026.345142, 2026.

Zhao, M., Eglinton, G., Read, G., and Schimmelmann, A.: An alkenone (U37K′) quasi-annual sea surface temperature record (A.D. 1440 to 1940) using varved sediments from the Santa Barbara Basin, Organic Geochemistry, 31, 903–917, https://doi.org/10.1016/S0146-6380(00)00034-6, 2000.

Zuhr, A. M., Dolman, A. M., Ho, S. L., Groeneveld, J., Löwemark, L., Grotheer, H., Su, C.-C., and Laepple, T.: Age-Heterogeneity in Marine Sediments Revealed by Three-Dimensional High-Resolution Radiocarbon Measurements, Front. Earth Sci., 10, 871902, https://doi.org/10.3389/feart.2022.871902, 2022.

~~Code and Data Availability~~

~~The dataset has been submitted to Pangaea and will be available under DOI __________, the code used to process analyse the files and will be made available on zenodo (https://doi.org/10.5281/zenodo.17352962).~~

~~Acknowledgements~~

~~We thank the scientists, technicians and support staff of cruises MV1012 and SPR0901 for the retrieval of the core material and especially Richard Norris and Janina Groninga for sampling the cores at Scripps Institution of Oceanography’s geological collection. Furthermore we would like to thank Jenny Altun and Susanne Alfken for lab training and help during the measurements, as well as Weimin Liu for invaluable help during processing. LLMs have been used to improve flow of text, as well as to correct grammar and spelling.~~

~~Financial support~~

~~This project has received funding from the European Research Council (ERC) under the European Union's Horizon 2020 research and innovation programme (grant agreement no. 716092). Additionally, this research was supported by Germany’s Excellence Strategy (EXC-2077) project 390741603 ‘The Ocean Floor – Earth’s Uncharted Interface’.~~